IET Renewable Power Generation

Special Issue Call for Papers

Be Seen. Be Cited.
Submit your work to a new IET special issue

Connect with researchers and experts in your field and share knowledge.

Be part of the latest research trends, faster.

Read more

The Institution of Engineering and Technology

Received: 1 December 2020 | Revised: 22 February 2021 | Accepted: 24 March 2021

IET Renewable Power Generation

DOI: 10.1049/rpg2.12184

The Institution of Engineering and Technology WILEY

ORIGINAL RESEARCH PAPER

Theoretical investigation on an oscillating buoy WEC-floating breakwater integrated system

Dezhi Ning[1,2] | Baoming Guo[1] | Rongquan Wang[1] | Lin Lin[2]

[1] State Key Laboratory of Coastal and Offshore Engineering, Dalian University of Technology, Dalian, China

[2] Science and technology research institute, China Three Gorges Corporation, Beijing, China

Correspondence
Rongquan Wang, State Key Laboratory of Coastal and Offshore Engineering, Dalian University of Technology, Dalian 116024, China.
Email: rqwang@dlut.edu.cn

Funding information
This work is supported by the National Natural Science Foundation of China (Grant Nos. 52001054 and 52011530183), Scientific Foundation of China Three Gorges Corporation (Grant No.201166740004) and China Postdoctoral Science Foundation (Grant No. 2019TQ0048)

Abstract

Based on the concept of cost sharing, an oscillating buoy wave energy converter- floating breakwater integrated system is proposed, in which the surge or pitch motion of the front-pontoon equipped with Power Take-off (PTO) system is allowed. In this study, the methods of eigenfunction matching and variables separation are applied to establish a theoretical model on hydrodynamic performance of the proposed integrated system. Under the condition of optimal PTO damping, the effects of the front-pontoon width, draft and pontoon spacing on the capture width ratio, reflection coefficient and transmission coefficient are investigated, respectively. It is found that the integrated system with surging front-pontoon performs better on the wave energy conversion than that with pitching one, especially in the high frequency region. The peaks of capture width ratio C_w are associated with the gap resonance and the increase of front-pontoon motion induced by the 'hydrodynamic constructive effect'.

1 | INTRODUCTION

A variety of technologies and concepts of wave energy conversion have been proposed in recent decades [1, 2]. However, limited by the variability and complexity of ocean waves, only a few wave energy converters (WECs) achieved the full-scale prototype test, or, reached the full-scale demonstration stage up to now. According to working principle, WECs can be classified as oscillating buoy (OB), oscillating water column (OWC) and overtopping devices [1]. Among which, the OB WECs as offshore devices are capable to harness more plentiful wave energy in deep sea. The typical single-body OB WEC is composed of an oscillating buoy, Power Take-off system and mooring system, by which wave energy is extracted from wave-induced buoy motions. However, offshore devices mean that more difficulties, such as installation, maintenance and placement of electricity storage component, need to be solved. Therefore, it is of practical significance to improve the configurations of single-body OB WECs.

Massive studies for OB WECs have been performed since the first oil crisis happened. Early theoretical research on the hydrodynamic characteristics of OB WECs is mostly based on linear potential theory. Evans [3] and Mei [4] derived the optimum conversion efficiency of 2D WECs for one degree of freedom (DOF), and they gave the optimizing criteria that the WEC needs to be adjusted to resonance and the PTO damping must equal to the hydrodynamic radiation damping. Mei [4], Budal [5] and Newman [6] further discussed the optimum conversion efficiency of 3D WECs. Based on those definitions and theoretical studies on OB WECs, many researchers explored the effects of buoy shapes and PTO system on the hydrodynamic performance, such as Mavrakos & Katsaounis [7] and Zhang et al. [8]. To resolve installation problems in deep water or large tidal region, two-body or multi-body systems are proposed, which were theoretically studied by Falnes [9] in detail. One representative study was undertaken by Yeung et al. [10–12], who proposed a dual coaxial-cylinder WEC and investigated systematically the effects of geometric parameters, outer shape

and PTO system on its energy conversion ability based on the theoretical derivations and experimental tests. Commonly, recent works on the two-body systems are focused on adaptability and survivability in complex and variable ocean environment [13–15]. In addition, some other OB WECs extracting wave energy from their relative rotation were proposed, such as Pelamis devices [16], PS FrogMk5 [17], Oyster [18] and so on.

However, compared with other renewable energy (such as solar, tidal and wind energy) technologies, wave energy technologies are still immature and demand relatively higher manufacturing, constructing and installing costs. At present, one promising solution to reduce budget is to integrate stand-alone devices into breakwaters, which significantly promotes the commercialization process of wave energy exploitation. In fact, the integrated system is not only beneficial for cost and space sharing, but have the potential to enhance the energy conversion ability of WECs [19]. According to categories of WECs, those integrated systems mainly consists of OWC WEC-breakwater and OB WEC-breakwater integrated systems.

Ojima et al. [20] first proposed an OWC WEC-fixed caisson breakwater hybrid system, then Takahashi [21] and Raju & Neelamina [22] discussed the reliability and stability of the integrated system thoroughly. An alternative OWC device with an additional seaward wall, namely U-shaped OWC device, integrated into the caisson breakwater was proposed and studied by Boccotti [23], Arena et al. [24] and Malara & Arena [25]. Martins-rivas & Mei [26] and Zheng et al. [27] established analytical models based on linear potential theory to investigate the hydrodynamic performance of a cylindrical OWC embedded into the straight coast/breakwater and found that the coastal effect can significantly enhance the power output performance of the OWC WEC. Moreover, an OWC device-floating breakwater integrated system was proposed by Neelamani et al. [28], who discussed the wave reflection, transmission and pneumatic efficiency of this system under the tidal effect in the deep water. He et al. [29] proposed A pile-supported OWC-breakwater integrated system and analytically investigated its hydrodynamic performance. Also, A floating box-type breakwaters with dual pneumatic chambers was reported by He et al. [30–32].

With regard to the OB WEC-breakwater, Ning et al. [33, 34] proposed a heaving floating box breakwater-WEC integrated system, and theoretically and experimentally investigated the effects of geometrical parameters and PTO damping on the reflection coefficient, transmission coefficient and capture width ratio. They reported that both the effective coastal protection and wave energy extraction functions were achieved by the proposed integrated system. Successively, Ning et al.[35, 36] extended the integrated system into a dual-pontoon one whose theoretical maximum hydrodynamic efficiency can reach up to 0.8 and the effective frequency bandwidth (i.e., transmission coefficient $K_T < 0.5$, capture width ratio $C_w > 0.2$) is relatively wide in comparison with the previous single-pontoon system. More recently, Konispoliatis et al. [37] developed an analytical model to investigate the hydrodynamics of array of vertical axisymmetric floaters with arbitrary bottom in front of a vertical breakwater. To deal with the effect of rear breakwater, the image method was adopted so that the hydrodynamic problem can be transferred to one without the presence of breakwater. Meanwhile, the boundary approximation method was employed to discretize the floaters bottom. Their numerical results were focused on the effects of array configurations and bottom shapes of floaters on the wave exciting force and hydrodynamic coefficients. A parallel investigation was carried out by Konispoliatis & Mavrakos [38], demonstrating that the existence of vertical breakwater always exerts constructive effect on the energy conversion ability of the proposed system, regardless of incident wave angle, array configuration or inner spacing between floaters.

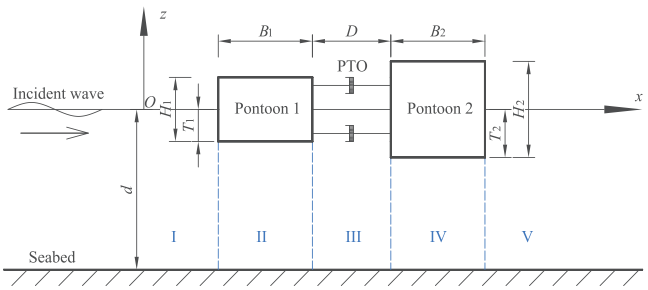

FIGURE 1 Sketch of the OB WEC-floating breakwater integrated system

To the authors' knowledge, most of the previous studies on WEC-breakwater integrated system were focused on OWC WEC-breakwater and heaving OB WEC-breakwater system. On the other hand, compared with bottom-mounted breakwater, the floating breakwater performs strong adaptability to weak geological conditions and reduces engineering cost in deep water and under large tide condition. Therefore, in this article, the OB WEC-floating breakwater integrated system is further investigated as an extension work of previous research by Ning et al. [36, 39]. In present model, the integrated system consists of dual rectangular pontoons and the seaward one is allowed to oscillate in surge or pitch mode. A theoretical model is developed based on linear potential flow theory to mainly investigate the energy conversion performance of the integrated system under different geometrical parameters. The objective of this study is to explore the variation of energy conversion efficiency with wavenumber or geometrical parameters in principle.

This work is organized as follows: Section 2 formulates the diffraction and radiation problems. Section 3 compares the present numerical results with theoretical relations given in published literatures. And then Section 4 displays and discusses the effects of front-pontoon width, draft and pontoon spacing on the hydrodynamic performance of the proposed system systematically. Finally, Section 5 draws the key conclusions.

2 | MATHEMATICAL MODEL

The schematic diagram of the OB WEC - floating breakwater integrated system is shown in Figure 1. The front rectangular pontoon is allowed to surge or pitch. It is considered that the integrated system dimension along the wave-crest line (y-axis, i.e., perpendicular to the wave propagation direction) is much

longer than the wavelength, thus a two-dimensional Cartesian coordinate (Oxz) system is employed, whose origin (O) is set on the undisturbed free surface, x-axis positive in the propagation direction of incident wave, and z-axis positive upwards. d is the water depth; B_n, T_n and H_n denote the width, draft and height of the front-pontoon respectively; D is the spacing between pontoon 1 and 2. The PTO system is applied to extract the wave energy from surge or pitch motion of the front-pontoon.

It is assumed that the fluid is inviscid, incompressible and the flow is irrotational, so the fluid field can be described by the velocity potential Φ. Also, all time-dependent variables are assumed to be harmonic,

$$\Phi(x, z, t) = \mathrm{Re}\left[\phi(x, z)\, e^{-\mathrm{i}\omega t}\right] \tag{1}$$

where Re denotes the real part of a complex number, t the time, $\mathrm{i} = \sqrt{-1}$ the imaginary unit, and ω the angular frequency. ϕ is complex velocity potential satisfying the Laplace equation,

$$\frac{\partial^2 \phi}{\partial x^2} + \frac{\partial^2 \phi}{\partial z^2} = 0 \tag{2}$$

The total velocity potential can be decomposed into three components for the linear system,

$$\phi = \phi_{\mathrm{I}} + \phi_{\mathrm{D}} + \phi_m \tag{3}$$

where ϕ_{I} is the incident velocity potential, ϕ_{D} the diffraction velocity potential; ϕ_m is the radiation velocity potential due to the motion of the front-pontoon in m mode. $m = 1$ and 3 represent surge and pitch modes, respectively. The incident velocity potential can be expressed as follow,

$$\phi_{\mathrm{I}} = -\frac{\mathrm{i}gA}{\omega}\frac{\cosh\left[k(z+d)\right]}{\cosh(kd)} e^{\mathrm{i}kx} \tag{4}$$

where A is the incident wave amplitude, and g is the gravity acceleration. k is the wavenumber satisfying the dispersion relation $\omega^2 = gk\tanh(kd)$.

The corresponding boundary conditions of all velocity potentials can be described as,

$$\begin{cases} \dfrac{\partial \phi_m}{\partial z} - \dfrac{\omega^2}{g}\phi_m = 0 \quad \left(z = 0, x < x_{l,1} \text{ or } x_{r,1} < x < x_{l,2} \text{ or } x > x_{r,2}\right) \\ \dfrac{\partial \phi_m}{\partial z} = 0 \quad \left(z = -d\right) \\ \dfrac{\partial \phi_m}{\partial z} = \mathrm{i}\omega\delta_{i,1}(x - x_0)\,\xi_3\delta_{3,m} - \dfrac{\partial \phi_I}{\partial z}\delta_{0,m} \quad \left(z = -T_i,\ x_{l,i} < x < x_{r,i},\ i = 1,\ 2\right) \\ \dfrac{\partial \phi_m}{\partial x} = -\mathrm{i}\omega\delta_{i,1}\left[\xi_1\delta_{1,m} + (z - z_0)\,\xi_3\delta_{3,m}\right] - \dfrac{\partial \phi_I}{\partial x}\delta_{0,m} \\ \qquad \left(-T_i < z < 0,\ \ x = x_{r,i} \text{ or } x = x_{l,i},\ i = 1,\ 2\right) \\ \lim\limits_{x\to\pm\infty}\left\{\dfrac{\partial}{\partial x} \mp ik\right\}\phi_m = 0 \end{cases} \tag{5}$$

in which $x_{\mathrm{r},i}$ and $x_{\mathrm{l},i}$ ($i = 1$ and 2) denote the horizontal coordinate values of right and left boundaries of the i-th pontoon, respectively. ξ_1 and ξ_3 are the complex motion response amplitude in surge and pitch modes. $\boldsymbol{C}_0 = (x_0, z_0)$ is the rotational centre of the front-pontoon. To simplify and unify the boundary conditions, ϕ_0 (i.e., when $m = 0$) is introduced to represent the diffraction velocity potential ϕ_{D}.

$$\delta_{p,q} = \begin{cases} 1 & p = q \\ 0 & p \neq q \end{cases} \tag{6}$$

The analytical expressions of all velocity potentials are given by the method of variables separation in each subdomain plotted in Figure 1, namely I, II, III, IV and V. Then, the eigenfunction matching method is employed to determine the unknown coefficients in analytical expressions. To be specific, those expressions are matched on the interfaces of adjacent subdomains based on the continuous conditions of the velocity potential and the horizontal velocity [36, 39]. Hence, the explicit forms of all velocity potentials are obtained. The horizontal exciting force and the rotational exciting moment can then be calculated by,

$$F_m = \mathrm{i}\omega\rho\int_S (\phi_{\mathrm{I}} + \phi_{\mathrm{D}})\, n_m \mathrm{d}s \tag{7}$$

where F_m denotes the generalized wave exciting force of the front-pontoon in m mode, ρ the fluid density, S the wetted surface of the front-pontoon, and n_m is the generalized normal direction. Note $n_1 = n_x$ and $n_3 = (z - z_0)n_x - (x - x_0)n_z$, and $\boldsymbol{n} = n_x\mathbf{i} + n_z\mathbf{k}$ is the unit normal vector on the pontoon surface pointing into the body.

The generalized wave force resulting from radiation potential due to unit-surge or unit-pitch motion is decomposed into two parts related to the added mass (proportional to the front-pontoon motion acceleration) and the radiation damping (proportional to the front-pontoon motion velocity), which can be calculated by,

$$\mu_m = \rho\int_S \mathrm{Re}\left[\varphi_m\right] n_m \mathrm{d}s \tag{8}$$

$$\lambda_m = \rho\omega\int_S \mathrm{Im}\left[\varphi_m\right] n_m \mathrm{d}s \tag{9}$$

where $\phi_m = -i\omega\varphi_m\xi_m$; μ_m and λ_m are the added mass and the radiation damping of the front-pontoon in m mode induced by a unit-amplitude motion of the front-pontoon in m mode, respectively.

Finally, the equation of motion for the integrated system can be written as,

$$\left(-\omega^2(M_m + \mu_m) - \mathrm{i}\omega(\lambda_m + \lambda_m^{PTO}) + K_m\right)\xi_m = F_m \tag{10}$$

where M_m and K_m are the mass and stiffness of the integrated system in m mode ($m = 1$, 3), respectively; λ_m^{PTO} is the PTO

damping in m mode. In this study, λ_m^{PTO} is selected to be the optimal PTO damping [36, 39],

$$\frac{\partial C_w}{\partial \lambda_m^{PTO}} = 0 \Rightarrow \lambda_m^{PTO} = \sqrt{\left(K_m/\omega - \omega\left(M_m + \mu_m\right)\right)^2 + \left(\lambda_m\right)^2}$$
$$M_1 = \rho B_1 T_1 \quad K_1 = \rho_1 g A_1$$
$$M_3 = I_{11}{}^b + I_{33}{}^b K_3 = \rho_1 g\left(I_{11}^{A_1} + I_3^{V_1}\right) - \rho B_1 T_1 g\left(z_c - z_0\right) \tag{11}$$

where $I_{11}{}^b$ and $I_{33}{}^b$ the rotational inertia of the first pontoon about $x = x_0$ and $z = z_0$, respectively, ρ_1, $A_1 = B_1$ and $V_1 = B_1 T_1$ the density of the first pontoon, water line and section area of underwater part of the first pontoon, respectively, I_{11}^{A} the quadratic moment of inertia of A_1 about $x = x_0$, $I_3^{V_1}$ the quadratic moment of inertia of V_1 about $z = z_0$. $\mathbf{Z_c} = (x_c, z_c)$ the centroid of the first pontoon.

The power P_{cap} absorbed by the integrated system in m mode is,

$$P_{cap} = \frac{1}{2}\omega^2 \lambda_m^{PTO} |\xi_m|^2 \tag{12}$$

According to the linear wave theory, the averaged energy flux per unit width P_{inc} in the incident wave can be expressed as,

$$P_{inc} = \frac{1}{4}\frac{\rho g A^2 \omega}{k}\left(1 + \frac{2kd}{\sinh 2kd}\right) \tag{13}$$

The capture width ratio C_w (i.e., energy conversion efficiency) is defined as a ratio of the captured wave energy against the incident wave energy per unit width,

$$C_w = \frac{P_{cap}}{P_{inc}} \tag{14}$$

The reflection coefficient K_R and transmission coefficient K_T of the breakwater can be calculated by,

$$K_R = \left| \frac{\phi_D + \phi_m}{\phi_I} \Big|_{\substack{z=0 \\ x=-\infty}} \right| \tag{15}$$

$$K_T = \left| \frac{\phi_I + \phi_D + \phi_m}{\phi_I} \Big|_{\substack{z=0 \\ x=-\infty}} \right| \tag{16}$$

For $K_T < 0.5$, a floating breakwater is basically considered satisfactory for shore protection [32, 40]. A WEC is regarded as being in the effective working state [33, 36] for capture width ratio $C_w > 0.2$ taking the energy losses in real engineering application. Therefore, the effective frequency bandwidth ($K_T < 0.5$, $C_w > 0.2$) is used to assess the overall performance of the proposed system. From the perspective of structural safety, this paper also defines the dimensionless free-surface elevation at the centre between pontoon 1 and 2 as,

$$A_c = \frac{A_{center}}{A} \tag{17}$$

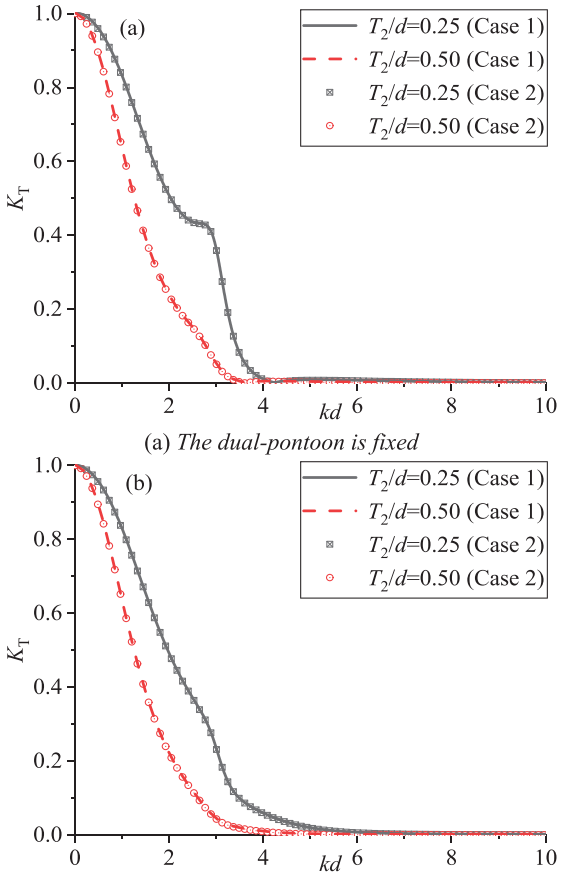

(a) *The dual-pontoon is fixed*

(b) *The first pontoon is allowed to surge to capture energy with the optimal* PTO *damping*

FIGURE 2 Variations of the transmission coefficient for the dual-pontoon versus the dimensionless wavenumber *kd*. Case 1 representing the incident wave from left to right, Case 2 representing the incident wave from right to left

3 | MODEL VALIDATION

To validate the proposed analytical model on the diffraction potential, radiation potential and the energy conversion performance, three examples are carried out. With regard to the diffraction potential, Kreisel [41] derived that the transmission coefficient in diffraction potential field is independent of the direction of the incident wave even though the body may not possess any symmetry at all. So the present model can be validated by comparing the transmission coefficient between two cases, that is, (1) an incident wave from left to right (2) an incident wave from right to left. Figure 2(a) shows the comparisons of the present model on K_T in diffraction potential field, in which the geometrical parameters are set as $B_1/d = 0.2$, $B_2/d = 0.6$, $T_1/d = 0.125$, $T_2/d = 0.25$ and 0.5, $D/d = 0.2$. It can be seen that the calculated results of two incident directions

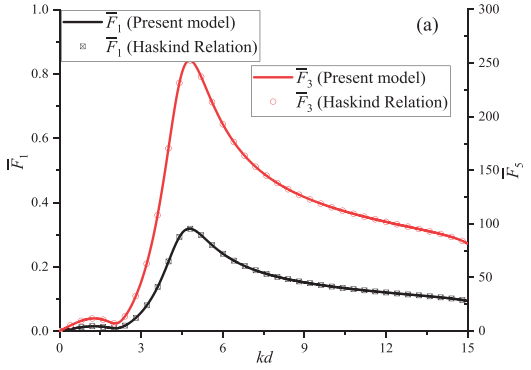

(a) *Comparisons of the present model on the wave exciting force with Haskind Relation* ($\overline{F}_1 = |F_1| / \rho g d A$ *and* $\overline{F}_3 = |F_3| / \rho g d B_1 A$)

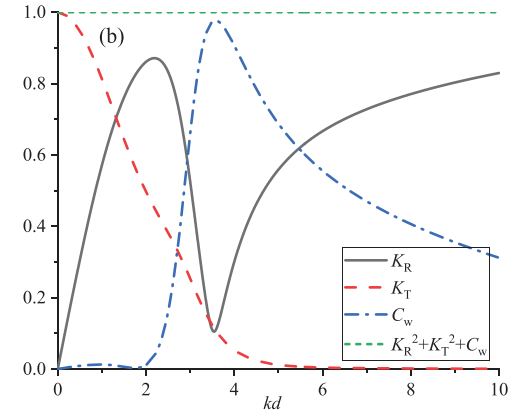

(b) *The related numerical results for the front-pontoon moving in surge and pitch modes.*

FIGURE 3 Variations of the generalized wave exciting force acting on the front-pontoon and $K_R^2 + K_T^2 + C_w$ with the wavenumber kd

are in good agreement, indicating that the present model can correctly solve the diffraction problem. In addition, Figure 2(b) shows the comparisons of the present dual-pontoon system on K_T when the first pontoon is allowed to surge to capture energy with the optimal PTO damping. Interestingly, K_T is still irrelevant to the incident wave direction whose proofs can be seen in [42]. However, K_T is different from the cases that the pontoons are both fixed due to the energy absorption of the moving front pontoon.

Furthermore, the Haskind Relation [43] is used to verify the correctness of the radiation potential due to the surge or pitch motion of front-pontoon. Figure 3(a) shows the variation of generalized wave exciting force with the dimensionless wavenumber. The geometrical parameters are $B_1/d = 10^{-4}$, $B_2/d = 0.6$, $T_1/d = T_2/d = 0.125$, $D/d = 0.2$, $H_1/T_1 = H_2/T_2 = 2$ and $\boldsymbol{C}_0 = [(x_{l,1} + x_{r,1})/2, -T_1]$. To illustrate that present model is still reliable for the integrated system with relatively small pontoon widths, the front pontoon B_1/d is set as 10^{-4}. Additionally, the power output associated with the surge and pitch motions is tested against the energy conservation relation of $K_R^2 + K_T^2 + C_w = 1$. Figure 3(b) shows the variation of K_R, K_T, C_w and $K_R^2 + K_T^2 + C_w$ with kd for $B_1/d = 0.3$, $B_2/d = 0.6$, $T_1/d = 0.125$, $T_2/d = 0.25$, $D/d = 0.2$. As shown in Figure 3(a,b), the present results fully satisfy those theoretical relations. Overall, the reliability of the present analytical model is well validated.

4 | NUMERICAL RESULTS AND DISCUSSIONS

The present study is mainly focused on the effects of the front-pontoon width, draft and pontoon spacing on the wave energy conversion for the integrated system with surging or pitching front-pontoon. In fact, it is found in this study that the hydrodynamic performances of the system with pitching and surging front-pontoon are similar to each other, which can be explained by the basically same physical mechanisms. Therefore, with regard to the pitching front-pontoon, this paper briefly describes the difference on hydrodynamic performance between pitch and surge motions. The study is carried out under the conditions of $B_2/d = 0.6$, $T_2/d = 0.25$, $H_1/T_1 = H_2/T_2 = 2$, $\boldsymbol{C}_0 = [(x_{l,1} + x_{r,1})/2, -T_1]$, $d = 10$ m and $g = 9.81$ m/s^2. Note that ξ_1 and ξ_3 are altered to respectively represent the dimensionless $|\xi_1|/A$ and $|\xi_3|/A$ in order to simplify the expression, ξ_1 and ξ_3 are named as surging and pitching RAO (response amplitude operator of the front-pontoon), respectively.

4.1 | System with the surging front-pontoon

4.1.1 | Effects of the front-pontoon width

For the surging front-pontoon, the effects of the width of front-pontoon on the hydrodynamic performance of the integrated system are firstly studied for different $B_1/d = 0.2$, 0.3, 0.4 and 0.6 in this subsection, maintaining $T_1/d = 0.125$ and $D/d = 0.2$. Figure 4 shows the variations of the reflection coefficient K_R, transmission coefficient K_T and capture width ratio C_w with dimensionless wavenumber kd for various widths of the front-pontoon. Also, K_R and K_T of the fixed isolated single pontoon ($B/d = 0.6$, $T/d = 0.25$) are plotted in Figure 4 to compare with the proposed integrated system with the WEC. The shape of the curve of K_R (or K_T, C_w) with kd for four front-pontoon widths are generally similar. It can be seen from Figure 4(a) that K_R decreases considerably when $kd > 2$ (relatively high frequency region) due to the existence of the surging front-pontoon (i.e., WEC), in which the reflection coefficient presents an obvious trough $K_R \approx 0$ near $kd = 3$ and the trough is shifted to the low frequency region with the increase of B_1. In Figure 4(c), C_w increases firstly to the peak $C_w \approx 1$ near $kd = 3$ and then decreases with the increase of kd. Additionally, the variation of peak of C_w with the width B_1 shows similar frequency shift phenomenon to the trough of K_R. Associated with that the reflection coefficient of isolated single pontoon does not present the decreasing trend, it is considered that the obvious trough region of K_R is because a certain amount of wave energy is extracted by the front-pontoon. In term of wave transmission K_T, with the increase of B_1, it slightly decreases in the range of $kd < 2$ and $kd > 4$, but increases in $2 < kd < 3$. Moreover, compared with

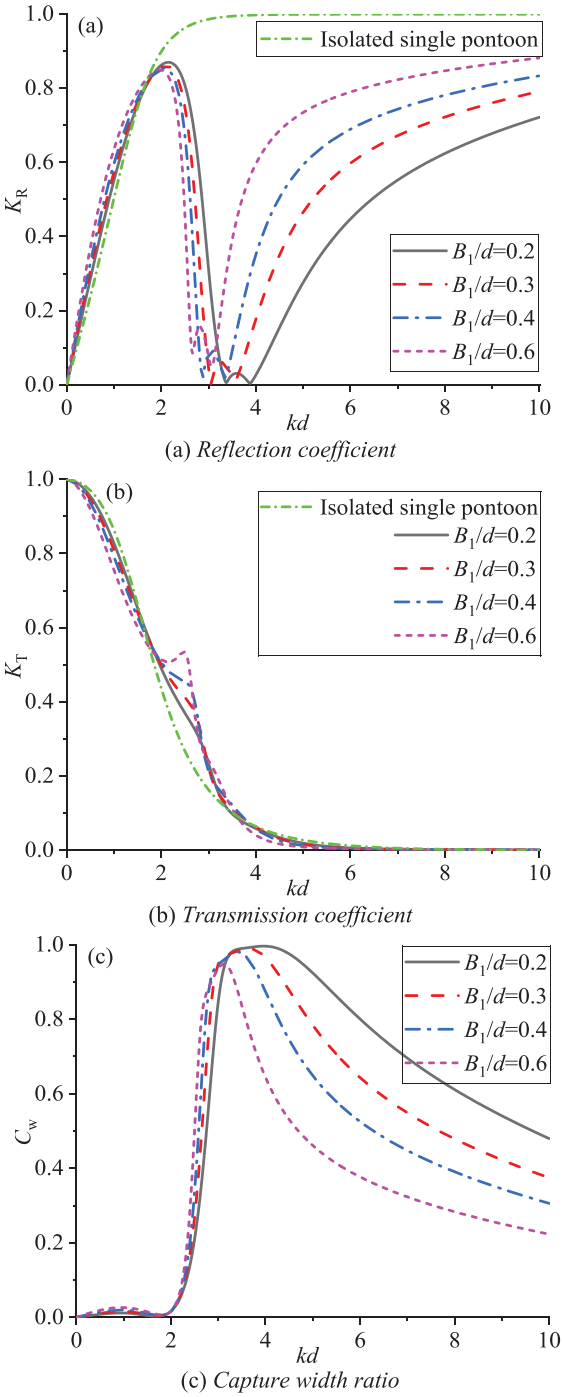

FIGURE 4 Variations of reflection coefficient K_R, transmission coefficient K_T and capture width ratio C_w versus the dimensionless wavenumber kd for various widths of the front-pontoon

the isolated single pontoon, the existence of front WEC leads to a larger K_T in the frequency region of $2 < kd < 3$.

To elaborate those phenomena on C_w, Figure 5 shows the variations of wave amplitude A_c between pontoons, wave exciting force $\overline{F}_1$, added mass μ_1, radiation damping λ_1 and surging RAO ξ_1 with kd for four widths of the front-pontoon. 'Only front-pontoon' means that the rear pontoon is removed from the integrated system(namely there is an isolated front-pontoon interacting with waves). It can be found from Figure 5(a,b) that the peaks of A_c and $\overline{F}_1$ are in the basically same frequency region, also the peaks gradually increase (becoming sharper and narrower) and shift to the low frequency region with the increase of B_1. Meanwhile, the added mass displays negative value and radiation damping sharply decreases in the corresponding frequency region to the peak region of A_c as shown in Figure 5(c). Therefore, it is confirmed that the enhancement of wave motion at gap between pontoons (gap resonance) leads to the increase of horizontal wave exciting force and the variations of μ_1 and λ_1. The surging RAO thus increases according to the equation of motion Equation (10), inducing the occurrence of the C_w peak. Moreover, it can be seen from Figure 4(c) that the capture width ratio can still reach up to 1 at frequency region ($4 < kd < 5.5$) which is far away from the peak of A_c, especially the small widths B_1. This is due to the 'hydrodynamic constructive effect', namely the combination of incident, diffraction and radiation potentials causing little reflection wave energy in this frequency region, so there is a relative large surging RAO ξ_1 near $kd = 4$ as shown in Figure 5(d). It should be noted that the current peak of ξ_1 is irrelevant to the surge-motion resonance. In fact, since the horizontal restore force is equal to zero, the front-pontoon cannot resonate in surge motion. To summarize, it is believed that the occurrence of the peak of capture width ratio C_w is dominated by the gap resonance between pontoons and the increasing front-pontoon motion. Obviously, the frequency shift phenomenon of C_w mentioned above is mainly because the frequency regions corresponding to the peak of A_c and ξ_1 both shift to the low frequency region with the increase of B_1.

The capture width ratio is close to zero in long wave region $kd < 2$ (i.e. low frequency region) as shown in Figure 4(c), demonstrating that the integrated system as a WEC mainly works in the intermediate and short waves. The reason is that most of the incident wave energy can transmit across the integrated system due to the strong transmission ability of long waves. As a result, the transmission wave amplitude is approximately equal to the incident wave amplitude. Thus, as illustrated in Figure 5(b), the wave exciting forces on the left and right sides of front-pontoon almost counterbalance (i.e. $\overline{F}_1 \approx 0$) in the range of $kd < 2$, which results in $C_w \approx 0$. In addition, it can be seen from Figure 4(c) that the peak value of C_w slightly increases with the decrease of B_1, and the effective bandwidth of C_w is significantly widened in the high frequency region of $kd > 5$. As the width B_1 increases, the wave exciting force basically maintains constant in the high frequency region as displayed in Figure 5(b), but the front-pontoon mass M_1 increase linearly. Thus, the surging RAO ξ_1 of a smallwidth pontoon is larger than that of a large one in high frequency region, leading to a relative wider effective bandwidth of C_w.

4.1.2 | Effects of the front-pontoon draft

Both the width ratio of the front-pontoon B_1/d and pontoon spacing ratio D/d are set as 0.2 to examine the effects of

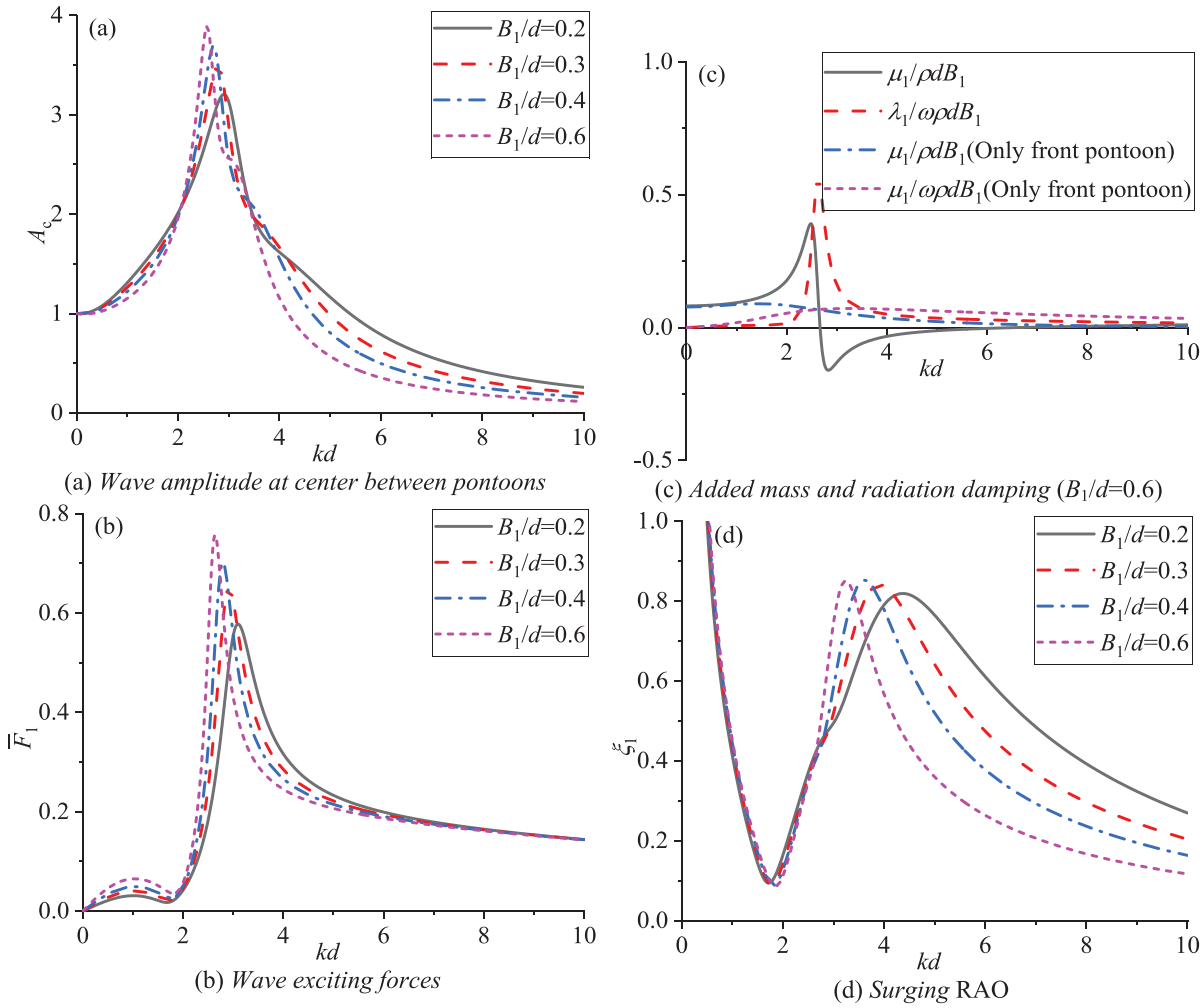

FIGURE 5 Variations of wave amplitude A_c between pontoons, wave exciting forces $\overline{F}_1$, added mass μ_1, radiation damping λ_1 and surging *RAO* of the front-pontoon ξ_1 versus the dimensionless wavenumber *kd for various widths of the front-pontoon*

front-pontoon draft on the energy conversion, taking T_1/d = 0.125, 0.2, 0.3 and 0.4, respectively. The variations of the reflection coefficient K_R, transmission coefficient K_T and capture width ratio C_w with the dimensionless wavenumber *kd* are plotted in Figure 6. It can be seen from Figure 6(a) that the variation of K_R with *kd* is similar to that mentioned above in Section 4.1.1. In particular, K_R shows two local troughs and an obvious local peak in the range of $2 < kd < 5$, which is different from that in Figure 4(a) where only one trough was observed. Also, the local peak and first trough (near kd = 2~3.5) of K_R both increase and shift to low frequency region with the increase of T_1, while the second trough occurring at about $kd = 4$ varies little with T_1.

Two local peaks (corresponding to the two local troughs of K_R) and a local trough (corresponding to the local peak of K_R) occur on the curves of C_w in the frequency range of $2 < kd < 5$. The explanation for this phenomenon is that the peak of A_c is gradually away from that of ξ_1 with the increase of T_1. Figure 7 shows the distributions of the wave amplitude A_c, surging RAO ξ_1 and optimal PTO damping λ_1^{PTO} with *kd*. As shown in Figures 7(a,b), the peaks of A_c and ξ_1 are near kd = 2.5 and 4, respectively. With increasing the draft T_1, the frequency left-shift of the peak of A_c due to the increase of water mass between pontoons is obviously greater than that of the peak of ξ_1, which means that the affected regions of the gap resonance and ξ_1 peak are gradually separated with the increase of T_1. The integrated system hence performs the weak energy conversion ability in the frequency region between the frequencies of A_c and ξ_1 peaks so that the local trough occurs on the curves of C_w and two local peaks appear. Obviously, the first local peak (or trough) of C_w (or K_R) is dominated by gap resonance and the second local peak is related to the peak of ξ_1. But it should be noted that the gap resonance inevitably affects the second local peak of C_w and the peak of ξ_1 affects the first one, which is the reason why frequencies of the local peaks of C_w are not exactly the same as those of the peaks of A_c or ξ_1. Additionally, the effect of the draft T_1 on ξ_1 is very limited in frequency region $2 < kd < 3$ as shown in Figure 7(b), while its effect on C_w is apparent as illustrated in Figure 6(c). The fact is that both the value and frequency of the peak of optimal

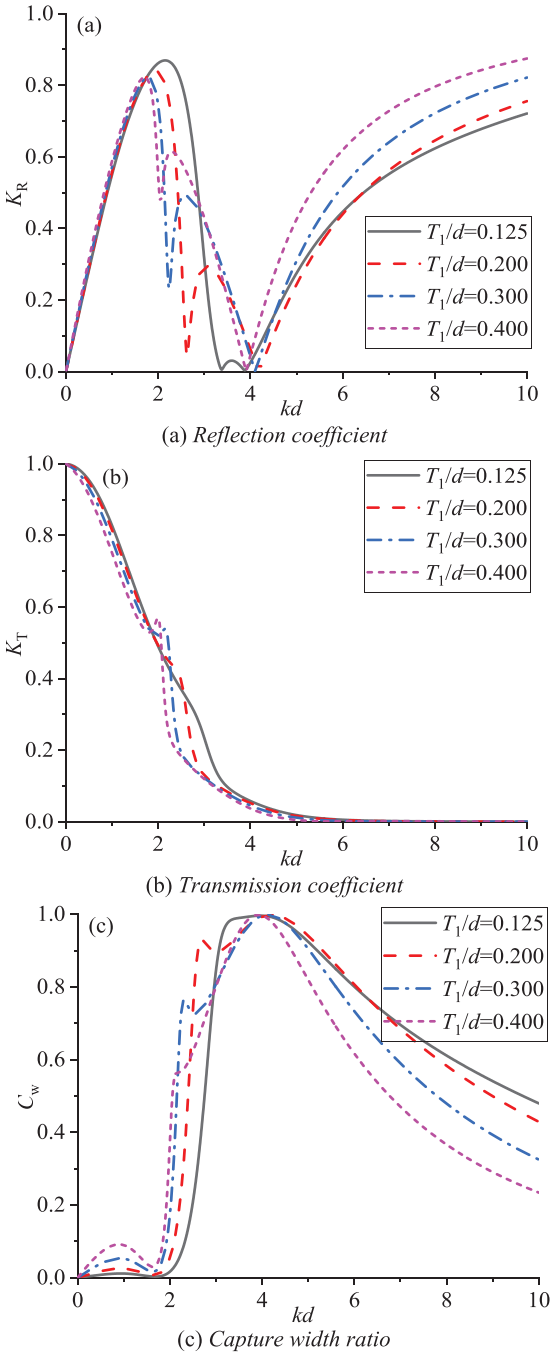

FIGURE 6 Variations of reflection coefficient K_R, transmission coefficient K_T and capture width ratio C_w versus the dimensionless wavenumber kd for various drafts of the front-pontoon

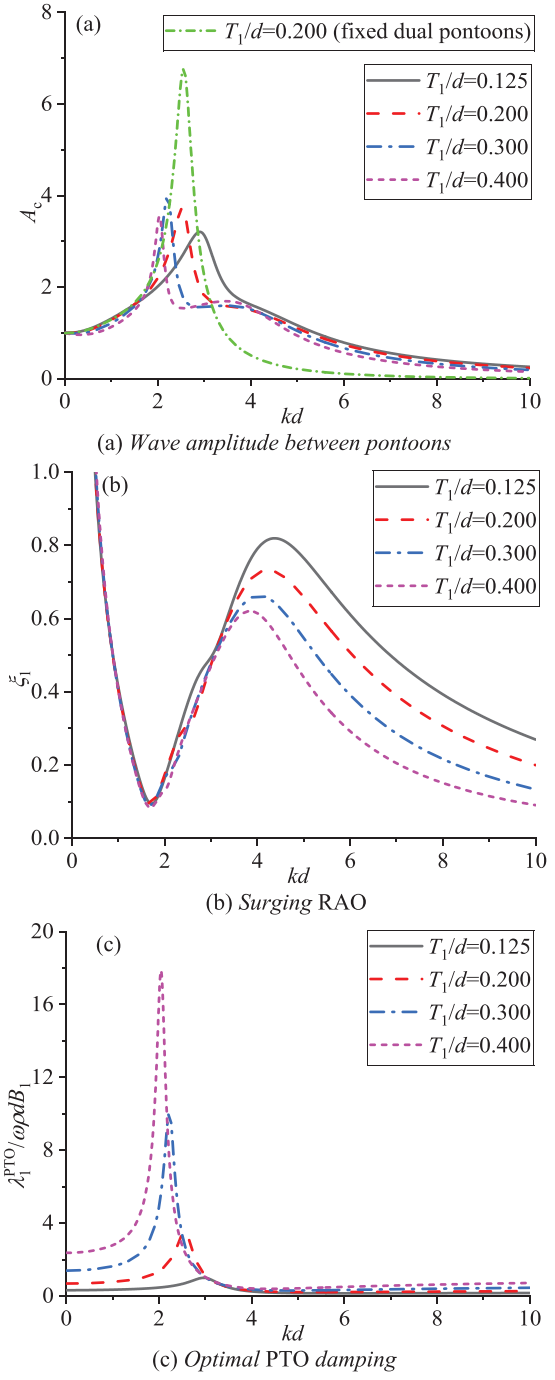

FIGURE 7 Variations of wave amplitude A_c between pontoons, surging RAO ξ_1 and optimal PTO damping λ_1^{PTO} versus wavenumber kd for various drafts of the front-pontoon

PTO damping λ_1^{PTO} are affected by the gap resonance. In view of structural safety, although the surge motion causes the increase of A_c in the range of $kd > 3$, A_c is less than 2, and it should be noted that the maximum wave amplitude A_c of the present system is significantly decreased at gap resonance frequency in comparison with 'fixed dual pontoons' due to the fact that some wave energy is captured by the surging front-pontoon. Overall, the proposed system can better satisfy the requirements of engineering safety.

It is found that the two local peaks of C_w (or the corresponding local troughs of K_R) are related to the zero points of the sum of front-pontoon mass M_1 and added mass μ_1. Figure 8 shows the variations of $G(\omega)$ with kd for four different front-pontoon drafts, in which $G(\omega) = M_1 + \mu_1$. There are just two zero points in $G(\omega)$ and the variations of them with the draft T_1 are similar to the two local troughs of K_R respectively. Table 1 gives precise frequencies corresponding to zero points of $G(\omega)$

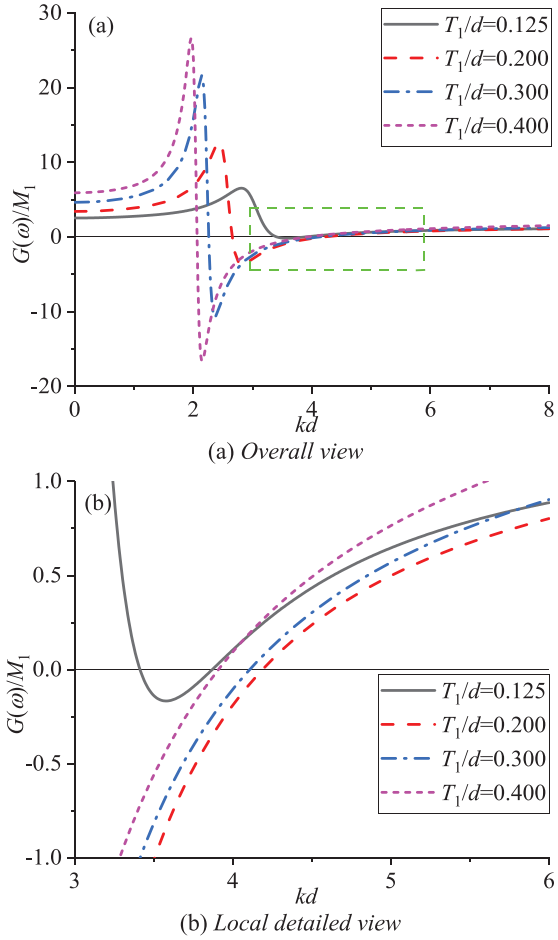

FIGURE 8 Variations of $G(\omega)$ versus the dimensionless wavenumber kd for various drafts of the front-pontoon

TABLE 1 Wavenumber kd corresponding to troughs of K_R and $G(\omega) = 0$ for four drafts T_1/d

The first local trough of K_R				
T_1/d	0.125	0.200	0.300	0.400
Troughs of K_R	3.376	2.624	2.240	2.048
$G(\omega) = 0$	3.416	2.656	2.264	2.064
The second local trough of K_R				
T_1/d	0.125	0.200	0.300	0.400
Troughs of K_R	3.880	4.184	4.104	3.912
$G(\omega) = 0$	3.872	4.192	4.104	3.912

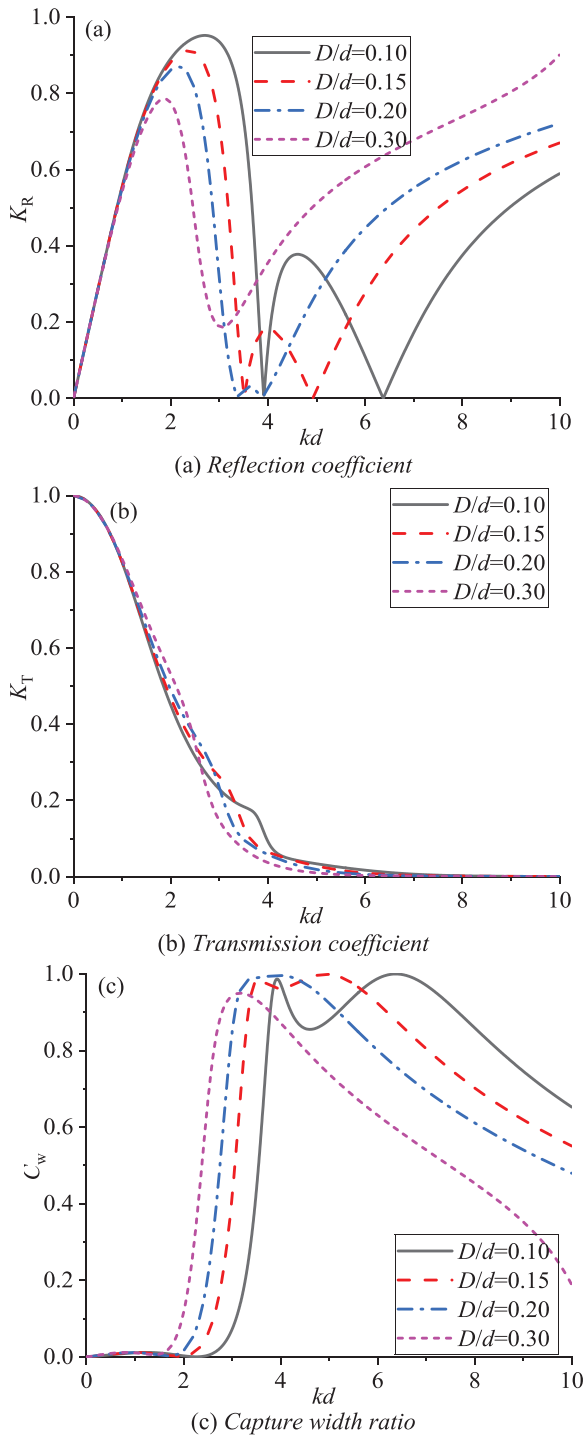

FIGURE 9 Variations of reflection coefficient K_R, transmission coefficient K_T and capture width ratio C_w versus the dimensionless wavenumber kd for various spacing D between pontoons

and local troughs of K_R. Whether the first or second trough, there is a little deviation between the corresponding frequencies to $G(\omega) = 0$ and to the local trough of K_R, especially the small drafts T_1. The deviation decreases with the increase of T_1, which is due to the weaker interaction between the gap resonance and ξ_1 peak. Overall, $G(\omega)$ can be employed to predict the local troughs of K_R and local peaks of C_w well.

4.1.3 | Effects of the pontoon spacing

The effects of the pontoon spacing D on the hydrodynamic performance are also studied under the conditions of $B_1/d = 0.2$ and $T_1/d = 0.125$. Figure 9 gives the variations of the reflection coefficient K_R, transmission coefficient K_T and capture

TABLE 2 Wavenumber kd corresponding to local troughs of K_R and $G(\omega) = 0$ for various spacing D/d

The first local trough of K_R				
D/d	0.10	0.15	0.20	0.30
Troughs of K_R	3.92	3.52	3.376	3.056
$G(\omega) = 0$	3.92	3.536	3.416	N/A
The second local trough of K_R				
D/d	0.10	0.15	0.20	0.30
Troughs of K_R	6.376	4.928	3.88	3.056
$G(\omega) = 0$	6.376	4.928	3.872	N/A

width ratio C_w versus dimensionless wavenumber kd for various pontoon spacing $D/d = 0.1$, 0.15, 0.2 and 0.3. As shown in Figure 9(a), the K_R curves show a similar oscillation phenomenon to that in Figure 6(a), in which K_R is considerably small in the intermediate frequency region and presents two local troughs and a local peak in general. With the increase of D, the local peak gradually decreases and even disappears for $D/d = 0.3$. Consequently, the two troughs merge into a single one. It can also be seen that all extreme points of K_R are obviously shifted to the low frequency region as D increases. C_w presents the corresponding local peaks and trough as given in Figure 9(c). Moreover, the effective frequency bandwidth of C_w decreases with the increase of D. With regard to the wave transmission, K_T slightly increases with the increasing D in the range of $1 < kd < 2.5$, and then presents an opposite variation trend as shown in Figure 9(b). Generally, the effect of pontoon spacing on wave transmission is very limited.

The decrease of the local peak of K_R (or the increase of the local trough value of C_w) is due to the fact that the peak frequency regions of A_c and ξ_1 are close to each other. The variations of wave amplitude A_c between pontoons and surging RAO ξ_1 with wavenumber kd are plotted in Figure 10 for various spacing D. It can be found that the peak of A_c and ξ_1 are both shifted to the low frequency region with the increase of D, in which frequency-shift distance of A_c is only 1.38 (i.e. the frequency difference of A_c peaks between $D/d = 0.1$ and 0.3), while that of ξ_1 is 2.97. It implies that the gap resonance frequency and peak frequency of ξ_1 gradually approach with the increasing D (though the peak frequency region of A_c and ξ_1 does not overlap fully), thus the wave energy conversion ability in the frequency region between the peaks of A_c and ξ_1 is enhanced, i.e., the local trough on the curve of C_w fades away. Similarly, the frequencies corresponding to local troughs of K_R and zero points of $G(\omega)$ for various spacing D are listed in Table 2. It can be seen that difference between the corresponding frequencies to $G(\omega) = 0$ and to the local trough of K_R slightly increases with the enhancement of interaction between gap resonance and ξ_1 peak as D increases. Unfavourably, for the largest spacing $D/d = 0.3$, zero points are not available in the curve of $G(\omega)$ in Figure 11, meaning that $G(\omega)$ is not applicable to predict the occurrence of the local troughs of K_R or local peaks of C_w for large pontoon spacing D/d.

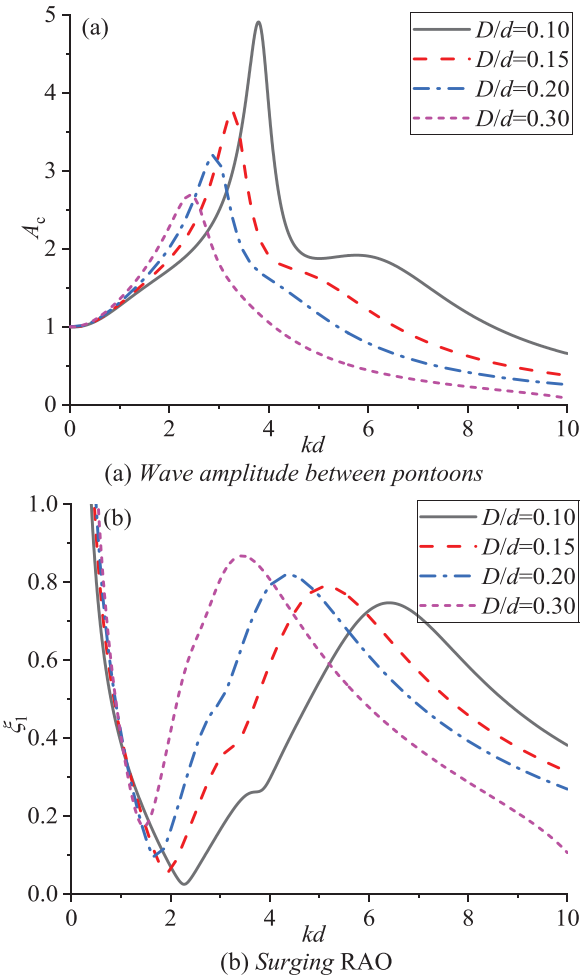

FIGURE 10 Variations of wave amplitude A_c between pontoons and surging RAO ξ_1 versus wavenumber kd for various spacing D between pontoons

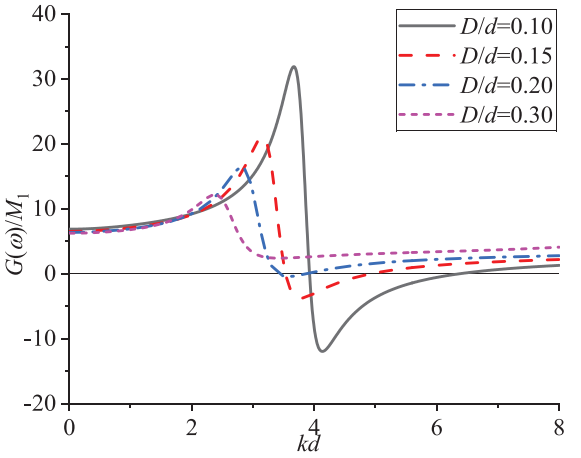

FIGURE 11 Variations of $G(\omega)$ versus the dimensionless wavenumber kd for various spacing D between pontoons

4.2 | System with the pitching front-pontoon

As mentioned above, the hydrodynamic performance of the integrated system with pitching front-pontoon is similar to that with surging one due to that both the two motions are anti-symmetric. Thus, this section only shows the effects of front-pontoon draft to discuss some extraordinary phenomena in the integrated system with pitching front-pontoon. The variations of the reflection coefficient K_R, transmission coefficient K_T and capture width ratio C_w with kd are depicted in Figure 12 for front-pontoon draft $T_1/d = 0.1$, 0.125, 0.2 and 0.25, and keeping $B_1/d = 0.5$ and $D/d = 0.2$.

As shown in Figures 12, K_R increases and K_T decreases with kd in the low frequency region (i.e. $kd < 2$) generally. For $kd > 2$, since a large amount of wave energy is absorbed by the WEC in the intermediate frequency region, C_w reaches up to its main peak near $kd = 3$ and K_R shows a trough region. The main peak of C_w is shifted to the low frequency region and its peak value decreases with the increase of T_1, and the effective frequency region of C_w becomes narrow at the same time. Furthermore, a sharp peak (hereafter named as sub-peak) occurs on the curve of C_w in the range of $kd < 2$ for a relatively small draft T_1 as shown in Figure 12(c). K_R and K_T also display similar extreme points at the same frequency points as illustrated in Figures 12(a,b). To clarify the variations of the main peak of C_w and the occurrence of sub-peak, Figure 13 gives the variations of wave amplitude A_c between pontoons and pitching RAO ξ_3 with kd for the corresponding drafts T_1. It can be seen that both the main peaks of A_c and ξ_3 are shifted to the low frequency region with the increase of T_1. Just as discussed in Section 4.1, the main peak of C_w thus shifts to the low frequency region. In addition, ξ_3 decreases obviously as T_1 increase in the range of $kd > 2.8$ as shown in Figure 13(b). Meanwhile, the peak shift distance of ξ_3 is larger than that of A_c, which causes peak frequency regions of A_c and ξ_3 further overlapping each other. The two aspects jointly lead the main peak of C_w and the effective frequency bandwidth of C_w to decrease with the increase of T_1.

It can be found that ξ_3 presents a sharp peak at the frequency corresponding to the sub-peak of C_w. The frequency is equal to the resonance frequency which can be calculated by $\omega_{res} = (K_1/(M_1+\mu_1))^{1/2}$. Therefore, it is confirmed that the occurrence of the sub-peak is due to the pitch-motion resonance. The restore moment decreases and the rotational inertia increases with the increase of draft T_1, which leads to a decreasing pitching resonance frequency for $T_1/d = 0.1$, 0.125 and 0.15 as shown in Figure 12(c). However, according to the formula of restore moment $K_1 = \rho g(B_1^2 - 6T_1^2)$, the restore moment is positive only when $B_1 > \sqrt{6}T_1$, so there is no sharp sub-peak on the curves of C_w for $T_1/d = 0.2$ and 0.25. With regard to the wave attenuation ability, the effect of T_1 on K_T is concentrated in intermediate frequency region $2 < kd < 5$ as shown in Figure 12(b). Because of the influence of gap resonance, K_T increases with increase of T_1 in the range of $2 < kd < 2.5$. However, the pitch motion of front-pontoon considerably decreases with increase of T_1 in $kd > 3$ as depicted by Figure 13(b), leading to the decrease of radiation waves, so K_T gradually decreases.

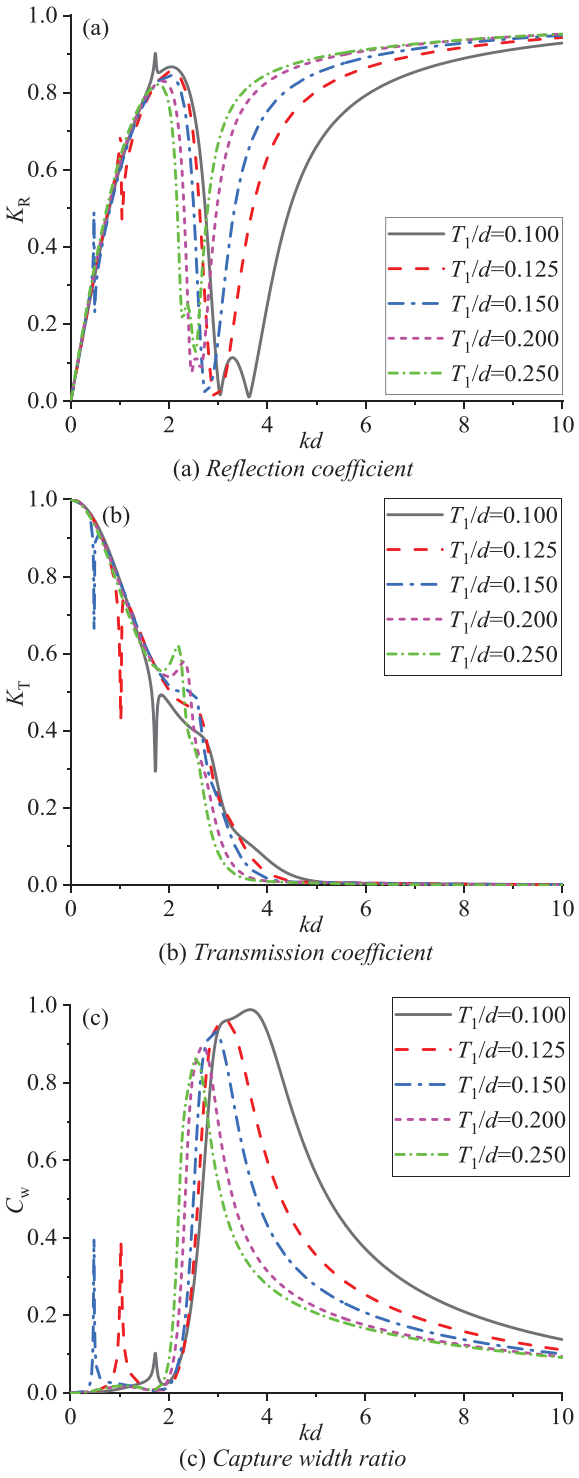

FIGURE 12 Variations of reflection coefficient K_R, transmission coefficient K_T and capture width ratio C_w versus the dimensionless wavenumber kd for various drafts of the front-pontoon

5 | CONCLUSIONS

The fixed floating breakwater with a movable front-pontoon is proposed as an OB WEC-breakwater integrated system. The front-pontoon is equipped PTO system to extract wave energy

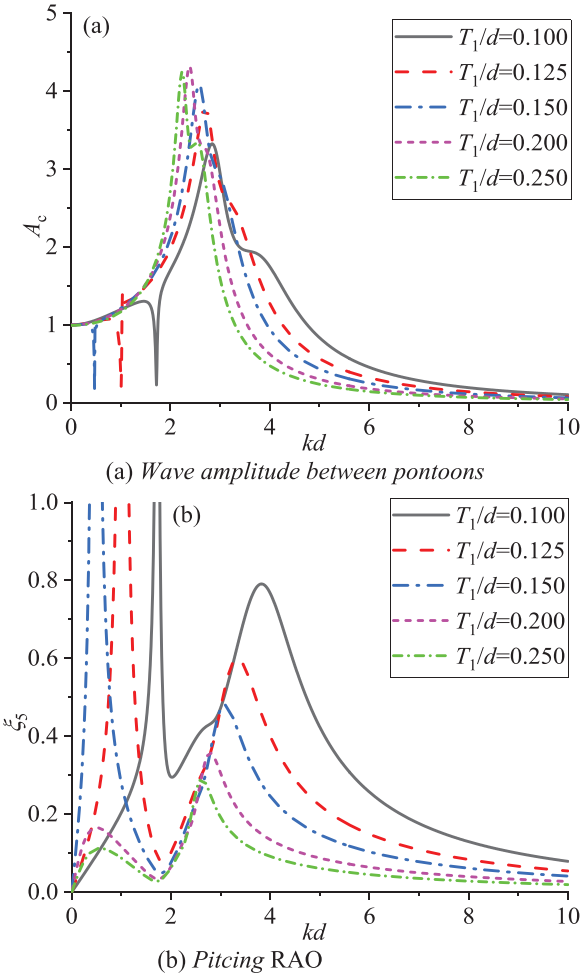

FIGURE 13 Variations of wave amplitude A_c between pontoons and pitching RAO ξ_3 versus wavenumber kd for various drafts of the front-pontoon

from its surge or pitch motion. Based on linear potential flow theory, the energy conversion performance of the integrated system is investigated by methods of eigenfunction matching and variables separation. In this paper, the effects of the front-pontoon width, draft and pontoon spacing on the reflection coefficient, transmission coefficient and capture width ratio are presented and discussed. Key conclusions are summarized as follows:

1. There are many similarities on the hydrodynamic performance between the integrated system with pitching front-pontoon and that with surging one. Their effective working frequency are both in the range of $kd > 2$ and the peaks of capture width ratio reach up to 1, that is, the reflected wave energy decreases considerably in this frequency region. Additionally, they are almost invalid on energy extraction from long waves and thus the ability to defence long waves have not been improved. However, the proposed system with surging front-pontoon is considerably superior to that with pitching one on energy conversion efficiency in the high frequency region. In view of this, this paper is mainly focused on the hydrodynamic performance of the integrated system with surging front-pontoon.

For integrated system with surging front-pontoon:

2. With the increase of the front-pontoon width, the effective frequency bandwidth gradually decreases and the peak of C_w is shifted to the low frequency region. It is found that the occurrence of peak of C_w is due to the gap resonance and the increase of front-pontoon motion resulted from 'hydrodynamic constructive effect'. Consequently, it is obvious that the frequency shift phenomenon of C_w peak is because the frequencies corresponding to peaks of A_c and ξ_1 are both shifted to the low frequency region with the increase of B_1.
3. As the draft of front-pontoon increases, two local troughs and a clear local peak appear on the curve of reflection coefficient, in which the first local trough and the peak of K_R increase and shift to the low frequency region, while the value and occurrence frequency of the second trough are almost kept constant. The capture width ratio presents the corresponding extreme points to K_R. That is because the frequency shift distance of gap resonance is relatively large, but that of peak of ξ_1 is small with the increase of T_1. In addition, it is found that $F(\omega) = M_1 + \mu_1 = 0$can be adopted to predict the occurrence frequencies of local peaks of C_w (or local troughs of K_R) in $2 < kd < 5$.
4. Since both the frequencies to peaks of A_c and ξ_1 are obviously shifted to the low frequency region with the increasing pontoon spacing D, the extreme points on the curve of C_w also shows the same shift phenomenon. Moreover, the peaks of A_c and ξ_1 are close to each other with the increase of D, causing the two local peaks of C_w merging and the effective frequency bandwidth of C_w decreasing.

ACKNOWLEDGEMENTS

This work is supported by the National Natural Science Foundation of China (Grant Nos. 52001054 and 52011530183), Scientific Foundation of China Three Gorges Corporation (Grant No.201166740004) and China Postdoctoral Science Foundation (Grant No. 2019TQ0048).

ORCID

Rongquan Wang https://orcid.org/0000-0002-5954-4585

REFERENCES

1. Falcão, A.F.D.O.: Wave energy utilization: A review of the technologies. Renewable Sustainable Energy Rev. 14, 899–918 (2010) https://doi.org/10.1016/j.rser.2009.11.003.
2. Qiu, S., et al.: A comprehensive review of ocean wave energy research and development in China. Renewable Sustainable Energy Rev. 113, 109271 (2019) https://doi.org/10.1016/j.rser.2019.109271.
3. Evans, D.V.: A theory for wave-power absorption by oscillating bodies. J. Fluid Mech. 77, 1–25 (1976) https://doi.org/10.1017/s0022112076001109.
4. Mei, C.C.: power extraction from water wave. J. Ship Res. 20, 63–66 (1976)
5. Budal, K.: Theory for Absorption of Wave Power by a System of Interacting Bodies. J. Ship Res. 21, 248–253 (1977)
6. Newman, J.N.: Absorption of wave energy by elongated bodies. Appl. Ocean Res. 1, 189–196 (1979)

7. Mavrakos, S.A., Katsaounis, G.M.: Parametric evaluation of the performance characteristics of tightly moored wave energy converters for several floaters' geometries. In: 8th European Wave and Tidal Energy Conference, Uppsala, Sweden (2009)
8. Zhang, W.C., et al.: Effect of linear and quadratic PTO on performance of vertical axisymmetric WEC. In: Proceedings of International Conference on Maritime Technology, Lisbon (2016)
9. Falnes, J.: Wave-energy conversion through relative motion between two single-mode oscillating bodies. J. Offshore Mech. Arct. 121, 32–38 (1999) https://doi.org/10.1115/1.2829552.
10. Chau, F.P., Yeung, R.W.: Inertia, damping, and wave excitation of heaving co-axial cylinders. In: Proceedings of the ASME 2012 31st International Conference on Ocean, Brazil (2012)
11. Cochet, C., Yeung, R.W.: Dynamic analysis and configuration design of a two-component wave-energy absorber. In: Proceedings of the ASME 2012 31st International Conference on Ocean, Brazil (2012)
12. Son, D., Belissen, V., Yeung, R.W.: Optimizing the performance of a dual coaxial-cylinder wave-energy extractor. In: Proceedings of the ASME 2015 34th International Conference on Ocean, Offshore and Arctic Engineering. Newfoundland, Canada (2015)
13. Xu, Q., et al.: Experimental and numerical investigations of a two-body floating-point absorber wave energy converter in regular waves. J. Fluids Struct. 91, 102613 (2019) https://doi.org/10.1016/j.jfluidstructs.2019.03.006.
14. Chen, Z.F., Zhang, L., Yeung, R.W.: Analysis and optimization of a Dual Mass-Spring-Damper (DMSD) wave-energy convertor with variable resonance capability. Renewable Energy 131, 1060–1072 (2019) https://doi.org/10.1016/j.renene.2018.07.006.
15. Yang, C., Zhang, Y.-L.: Numerical study of hydrodynamic behavior and conversion efficiency of a two-buoy wave energy converter. J. Hydrodyn. 30, 235–248 (2018) https://doi.org/10.1007/s42241-018-0025-6.
16. Pizer, D.J., et al.: Pelamis WEC—recent advances in the numerical and experimental modelling programme. Proceedings of 6th European Wave Tidal Energy Conference, Glasgow (2005)
17. McCabe, A.P., et al.: Developments in the design of the PS Frog Mk 5 wave energy converter. Renewable Energy 31, 141–151 (2006) https://doi.org/10.1016/j.renene.2005.08.013.
18. Whittaker, T., et al.: The development of Oyster—a shallow water surging wave energy converter. Proceedings of 7th European Wave Tidal Energy Conference. Porto, Portugal (2007)
19. Vicinanza, D., et al.: Innovative rubble mound breakwaters for overtopping wave energy conversion. Coastal Eng. 88, 154–170 (2014) https://doi.org/10.1016/j.coastaleng.2014.02.004.
20. Ojima, R., Suzumura, S., Goda, Y.: Theory and experiments on extractable wave power by an oscillating water-column type breakwater caisson. Coastal Eng. J. 27, 315–326 (1984)
21. Takahashi, S.: Hydrodynamic characteristics of wave-power-extracting caisson breakwater. Twenty-First Coastal Engineering Conference. New York, NY (1988)
22. Raju, J., Neelamina, S.: Concrete caisson for a 150 KW wave energy pilot plant. Design, construction and installation aspects. Proceedings of The Second Intemational Offshore and Polar Engineering Conference. San Francisco, California, USA (1992)
23. Boccotti, P.: On a new wave energy absorber. Ocean Eng. 30, 1191–1200 (2003) https://doi.org/10.1016/s0029-8018(02)00102-6.
24. Arena, F., Romolo, A., Malara, G.: On design and building of a U-OWC wave energy converter in the mediterranean sea: A case study. Proceedings of the ASME 2013 32nd International Conference. Nantes, France (2013)
25. Malara, G., Arena, F.: Response of U-Oscillating water column arrays: Semi-analytical approach and numerical results. Renewable Energy 138, 1152–1165 (2019) https://doi.org/10.1016/j.renene.2019.02.018.
26. Martins-rivas, H., Mei, C.C.: Wave power extraction from an oscillating water column along a straight coast. Ocean Eng. 36, 426–433 (2009) https://doi.org/10.1016/j.oceaneng.2009.01.009.
27. Zheng, S.M., Zhang, Y.L., Iglesias, G.: Coast/breakwater-integrated OWC: A theoretical model. Marine Struct. 66, 121–135 (2019) https://doi.org/10.1016/j.marstruc.2019.04.001.
28. Neelamani, S., Natarajan, R., Prasanna, D.L.: Wave Interaction With Floating Wave Energy Caisson Breakwaters. J. Coastal Res. 22, 745–749 (2006)
29. He, F., et al.: Hydrodynamic performance of a pile-supported OWC breakwater: An analytical study. Appl. Ocean Res. 88, 326–340 (2019) https://doi.org/10.1016/j.apor.2019.03.022.
30. He, F., Leng, J., Zhao, X.: An experimental investigation into the wave power extraction of a floating box-type breakwater with dual pneumatic chambers. Appl. Ocean Res. 67, 21–30 (2017) https://doi.org/10.1016/j.apor.2017.06.009.
31. He, F., Huang, Z., Law, A.W.-K.: Hydrodynamic performance of a rectangular floating breakwater with and without pneumatic chambers: An experimental study. Ocean Eng. 51, 16–27 (2012). https://doi.org/10.1016/j.oceaneng.2012.05.008.
32. He, F., Huang, Z., Law, A.W.-K.: An experimental study of a floating breakwater with asymmetric pneumatic chambers for wave energy extraction. Appl. Energy. 106, 222–231 (2013) https://doi.org/10.1016/j.apenergy.2013.01.013.
33. Ning, D.Z., et al.: Hydrodynamic performance of a pile-restrained WEC-type floating breakwater: An experimental study. Renewable Energy. 95, 531–541 (2016) https://doi.org/10.1016/j.renene.2016.04.057.
34. Zhao, X., et al.: Hydrodynamic investigation of an oscillating buoy wave energy converter integrated into a pile-restrained floating breakwater. Energies. 10, 712 (2017) https://doi.org/10.3390/en10050712.
35. Ning, D., et al.: Experimental investigation on hydrodynamic performance of a dual pontoon–power take-off type wave energy converter integrated with floating breakwaters. Proceedings of the Institution of Mechanical Engineers. J. Eng. Maritime Environ. 233, 991–999 (2018) https://doi.org/10.1177/1475090218804677.
36. Ning, D.Z., et al.: Analytical investigation of hydrodynamic performance of a dual pontoon WEC-type breakwater. Appl. Ocean Res. 65, 102–111 (2017) https://doi.org/10.1016/j.apor.2017.03.012.
37. Konispoliatis, D.N., Mavrakos, S.A., Katsaounis, G.M.: Theoretical evaluation of the hydrodynamic characteristics of arrays of vertical axisymmetric floaters of arbitrary shape in front of a vertical breakwater. J. Marine Sci. Eng. 8, 62 (2020) https://doi.org/10.3390/jmse8010062.
38. Konispoliatis, D.N., Mavrakos, S.A.: Wave power absorption by arrays of wave energy converters in front of a vertical breakwater: A theoretical study. Energies. 13, 1985 (2020) https://doi.org/10.3390/en13081985.
39. Zhao, X., et al.: Analytical study on an oscillating buoy wave energy converter integrated into a fixed box-type breakwater. Math. Probl. Eng. 2017, 1–9 (2017) https://doi.org/10.1155/2017/3960401.
40. Koutandos, E., Prinos, P., Gironella, X.: Floating breakwaters under regular and irregular wave forcing: Reflection and transmission characteristics. J. Hydraulic Res. 43, 174–188 (2010) https://doi.org/10.1080/00221686.2005.9641234.
41. Kreisel, G.: Surface waves. Quart. Appl. Math. 7, 21–44 (1949)
42. Zheng, S., Zhang, Y.: Analytical study on hydrodynamic performance of a raft-type wave power device. J. Marine Sci. Technol. 22, 620–632 (2017) https://doi.org/10.1007/s00773-017-0436-z.
43. Newman, J.N.: The exciting forces on fixed bodies in waves. J. Ship Res. 6, 10–17 (1962)

How to cite this article: Ning D, Guo D, Wang R, Lin L. Theoretical investigation on an oscillating buoy WEC-floating breakwater integrated system. IET Renew. Power Gener. 202115:;3472–3484. https://doi.org/10.1049/rpg2.12184.